A New Method of Adaptive Integration with Error Control for Bond-Based Peridynamics

Kebing Yu, X.J. Xin *, Kevin B. Lease

Abstract—**Peridynamics is a new formulation of solid mechanics and possesses some advantages in handling discontinuities within a continuum. Since the formulation is based on direct interactions between points in a continuum separated by a finite distance, integration of interactions between points plays a crucial role in peridynamics. This research is focused on developing a new method of numerical integration with error control for bond-based peridynamics. In this method, the continuum is discretized into cubic cells, and integration over full and partial cells in the horizon of interaction are calculated accurately. An adaptive trapezoidal integration scheme with a combined relative-absolute error control is employed. Numerical examples of areal force density for triaxial and pure shear loading show that the new method is much more accurate and efficient than the previous method published in the literature.**

Keywords: peridynamics, adaptive error control, trapezoidal integration

1 Introduction

Problems involving crack growth and damage are important in solid mechanics. The partial differential equations in the classic theory are incompatible with the discontinuities because the spatial derivatives needed by those equations are undefined along the crack tips or crack surfaces. A non-local theory called *peridynamics* has been developed by Silling in an attempt to overcome the aforementioned difficulty [1]. In peridynamics the classic partial differential equations are replaced with integral equations so that the same equations hold true anywhere in the body, including crack tips or surfaces.

The peridynamic theory has been applied successfully to crack and damage problems [2,3]. A meshfree method to numerically implement the peridynamic theory was proposed in [4]. The peridynamic theory also serves as a nice framework that allows the use of other constitutive models [5–8]. The convergence of peridynamics has been studied in [9, 10]. The peridynamic theory has also been advanced from the original bond-based peridynamics to state-based peridynamics [11] which removes the restriction of a constant Poisson's ratio of $\frac{1}{4}$ and introduces the classic concepts of stress and strain. These new developments also allow peridynamic theory to handle dynamic fracture problems [12, 13].

In the literature, the bond-based peridynamic theory has been focused mostly on dynamic material behavior rather than fundamental mechanics problems involving stress and strain calculations, and published methods of numerical integration [1, 4] yield poor stress results. In this work a new integration method is developed which allows for a more accurate integration of the governing equation in bond-based peridynamics. With this new method, the calculation of stresses and strains with predetermined accuracy can be achieved. The new method is verified with some well-defined elasticity problems with closed form solutions.

2 A Brief Review of Bond-Based Peridynamic Theory

Bond-based peridynamics [1, 4] assumes that the solid body is composed of small particles. Each particle interacts with others within a finite distance δ called the *horizon*. The pairwise interaction between two particles exists even when they are not in contact. This physical interaction is referred to as a *bond*, which in some way has a close analogy to a mechanical spring.

In bond-based peridynamics, the equation of motion for particle i in the reference configuration at time t is:

$$\rho\ddot{\mathbf{u}}(\mathbf{x}_i,\, t) = \int_{\mathscr{H}_i} \mathbf{f}\left[\mathbf{u}(\mathbf{x}_j,\, t) - \mathbf{u}(\mathbf{x}_i,\, t),\, \mathbf{x}_j - \mathbf{x}_i\right] dV_j + \mathbf{b}(\mathbf{x}_i,\, t), \quad \forall j \in \mathscr{H}_i \tag{1}$$

where $\mathscr{H}_i$ is a spherical neighborhood of particles that interacts with particle i, dV_j is an infinitesimal volume associated with particle j, $\mathbf{u}$ is the displacement vector field, $\mathbf{b}$ is a prescribed body force density field, ρ is the mass density, and $\mathbf{f}$ is the *pairwise peridynamic force* (henceforth referred to as the *bond force*) function whose value is the force vector (per unit volume squared) that particle j exerts on particle i.

There are two frequently used terms in peridynamic theory: the *relative position* $\boldsymbol{\xi}$ of two particles i and j in the reference configuration:

$$\boldsymbol{\xi} = \mathbf{x}_j - \mathbf{x}_i \tag{2}$$

*Department of Mechanical and Nuclear Engineering, Kansas State University, Manhattan, KS 66506 USA Email: xin@ksu.edu

ISBN: 978-988-18210-0-3
ISSN: 2078-0958 (Print); ISSN: 2078-0966 (Online)

and the *relative displacement* $\boldsymbol{\eta}$:

$$\boldsymbol{\eta} = \mathbf{u}(\mathbf{x}_j, t) - \mathbf{u}(\mathbf{x}_i, t) \tag{3}$$

So $|\boldsymbol{\xi}|$ and $|\boldsymbol{\eta}+\boldsymbol{\xi}|$ represent the initial and current length of the bond, respectively.

A simple and useful type of bond-based peridynamic material is called the *Prototype Microelastic Brittle* (PMB) material [4]. For a PMB material, the bond force function $\mathbf{f}$ is a linear function of the current bond stretch s, which also serves as the constitutive model:

$$\mathbf{f}(\boldsymbol{\eta}, \boldsymbol{\xi}) = \mu(\boldsymbol{\xi}) \frac{18K}{\pi\delta^4} \frac{\boldsymbol{\eta}+\boldsymbol{\xi}}{|\boldsymbol{\eta}+\boldsymbol{\xi}|} s \tag{4}$$

where K is the bulk modulus, and s is defined as:

$$s = \frac{|\boldsymbol{\eta}+\boldsymbol{\xi}| - |\boldsymbol{\xi}|}{|\boldsymbol{\xi}|} \tag{5}$$

and $\mu(\boldsymbol{\xi})$ is a history-dependent scalar-valued function that equals either 1 or 0:

$$\mu(\boldsymbol{\xi}) = \begin{cases} 1 & \text{for} \quad s < s_0 \\ 0 & \text{otherwise} \end{cases} \tag{6}$$

where s_0 is the critical bond stretch for bond failure.

The bond-based peridynamic theory can be related to classic elasticity theory through the concept of force per unit area. Assume an infinite body $\mathscr{R}$ undergoes a deformation. Choose a particle $\mathbf{x}$ and a unit vector $\mathbf{n}$ at $\mathbf{x}$ and let a plane pass through $\mathbf{x}$ to divide the whole body into two parts: $\mathscr{R}^-$ and $\mathscr{R}^+$:

$$\mathscr{R}^+ = \{\mathbf{x}' \in \mathscr{R} : (\mathbf{x}' - \mathbf{x}) \cdot \mathbf{n} \geq 0\} \tag{7}$$

$$\mathscr{R}^- = \{\mathbf{x}' \in \mathscr{R} : (\mathbf{x}' - \mathbf{x}) \cdot \mathbf{n} \leq 0\} \tag{8}$$

and let $\mathscr{L}$ be the following set of colinear points:

$$\mathscr{L} = \{\hat{\mathbf{x}} \in \mathscr{R}^- : \hat{\mathbf{x}} = \mathbf{x} - p\mathbf{n},\ 0 \leq p < \infty\} \tag{9}$$

The *areal force density* $\boldsymbol{\tau}(\mathbf{x}, \mathbf{n})$ at $\mathbf{x}$ in the direction of unit vector $\mathbf{n}$ is defined as [1]:

$$\boldsymbol{\tau}(\mathbf{x}, \mathbf{n}) = \int_{\mathscr{L}} \int_{\mathscr{R}^+} \mathbf{f}(\mathbf{u}' - \hat{\mathbf{u}}, \mathbf{x}' - \hat{\mathbf{x}}) dV_{\mathbf{x}'}\, d\hat{l} \tag{10}$$

where $d\hat{l}$ represents the differential path length over $\mathscr{L}$.

A meaningful representation of a stress tensor $\boldsymbol{\sigma}$ can be proposed [1]:

$$\boldsymbol{\tau}(\mathbf{x}, \mathbf{n}) = \boldsymbol{\sigma}\mathbf{n}, \quad \forall \mathbf{n} \tag{11}$$

This stress tensor is a Piola-Kirchhoff stress tensor since $\boldsymbol{\tau}(\mathbf{x}, \mathbf{n})$ is force per unit area in the reference configuration.

In the literature, a meshfree code named *EMU* [4] has been developed to numerically implement the peridynamic theory. In this implementation the domain of interest is discretized into a cubic lattice system. Each cubic cell contains a representative point at the mass center called *node*. Generally all cubes have the same size so all nodes together form a uniform grid system. The distance between two nearest neighboring nodes is called *grid spacing* (denoted as Δx).

For convenience, the node of interest is referred to as the *source node*. Based on the peridynamic theory, the *family nodes* of a source node is a set of nodes which have peridynamic interaction with the source node. Following the concept of horizon, the family nodes form a spherical neighborhood (henceforth referred to as the *horizon sphere*) centered at the source node with radius equals to horizon. A horizon of three times the grid spacing has been suggested in [4].

For numerical integration, the equation of motion at the source node i can be discretized to:

$$\rho\ddot{\mathbf{u}}_i = \sum_j \int \mathbf{f}(\boldsymbol{\eta}, \boldsymbol{\xi})\, dV_j + \mathbf{b}_i,\ \forall j \in \mathscr{H}_i \tag{12}$$

where $\mathscr{H}_i$ is the horizon sphere of node i. For each family node j in $\mathscr{H}_i$, the integration is carried out over the cell volume of node j which may be fully or partially in the horizon sphere. Equation (12) is the discretized form of equation of motion corresponding to Eqn. (1).

Because the principle of bond-based peridynamics involves only two-particle interactions, it is inevitable that all bond-based peridynamic materials have a fixed Poisson's ratio of $\frac{1}{4}$ [1]. A further development of the theory removes this restriction [11].

3 Deficiencies in the Existing Numerical Implementation of Peridynamics

There are two deficiencies in the existing implementation of peridynamics presented in [1, 2, 4] that may prevent it from achieving accurate and consistent results:

(1) Theoretically, all material points in the horizon sphere should be included in the calculation of bond forces. The implementation in [2, 4], however, counts each cell as either entirely in or entirely out of the horizon, and thus results in an inaccurate accounting of material points. Consider a grid of $\Delta x = \delta/3$. Figure 1A shows all the family nodes (solid dots) counted by the existing implementation [2, 4] in a projection view where the circle represents the horizon sphere and the square grids represent the cells of the nodes. Because only cells with their center nodes in the horizon sphere (solid dots) are considered family nodes, the partial cell areas (denoted with horizontal line pattern) whose center nodes are located outside the horizon sphere (open dots) are omitted. Since the omitted volume contains material points that are part of the horizon sphere, the summation in Eqn. (12) excludes partial cell volumes represented by open dots. Grid refinement may reduce the error, but the problem remains.

ISBN: 978-988-18210-0-3
ISSN: 2078-0958 (Print); ISSN: 2078-0966 (Online)

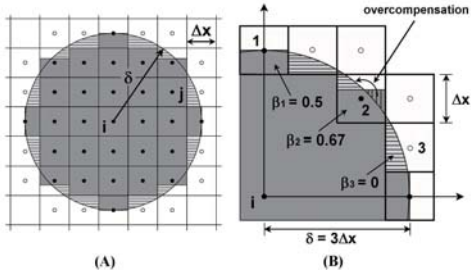

Figure 1: (A) Accounting of the family nodes by the numerical implementation presented in [2, 4]; (B) The volume of the quarter horizon sphere calculated by the cubic-cell integration.

(2) The three-dimensional integration in Eqn. (12) is performed using a one-point integration [2, 4, 14]:

$$\rho\ddot{\mathbf{u}}_i = \sum_j \left[\mathbf{f}(\boldsymbol{\eta},\, \boldsymbol{\xi}) \cdot \beta(\Delta x)^3\right] + \mathbf{b}_i \qquad (13)$$

where $(\Delta x)^3$ is the cell volume and β is the *volume reduction factor* defined as:

$$\beta = \begin{cases} 1 & \text{for} \quad |\boldsymbol{\xi}| \le \delta - 0.5\Delta x \\ \dfrac{\delta + 0.5\Delta x - |\boldsymbol{\xi}|}{\Delta x} & \text{for} \quad |\boldsymbol{\xi}| \le \delta + 0.5\Delta x \\ 0 & \text{otherwise} \end{cases} \qquad (14)$$

For convenience, the integration method implemented in [1, 2, 4] is referred to as *cubic-cell integration*. Figure 1B illustrates the cubic-cell integration method when $|\boldsymbol{\xi}|$ is within the range of δ-$0.5\Delta x$ and δ+$0.5\Delta x$, *i.e.*, the cubic cell is partially in the horizon sphere. In the figure, the circular arc represents a quarter of the horizon sphere. The volume of the quarter sphere calculated by the cubic-cell integration is marked as the dark shaded area. The volume missed in the calculation is marked as the horizontal line patterned area. For family node 1, a small extra volume is added to the actual intersection volume. For family node 2, the cubic-cell integration overcompensates the missing volume in the cell with the calculated volume (vertical slashed area). For node 3, since it is not counted as a family node, its cell contributes nothing to the integration. Partial cell volumes of three other nodes (represented by unnumbered open dots) in the figure are also excluded from the calculation. Such an approximation in counting the volume integration elements leads to poor accuracy of the numerical bond-based peridynamic model.

4 A New Method of Adaptive Integration with Error Control

The key to improving the accuracy in the numerical implementation of peridynamics is to evaluate the integration in Eqn. (12) properly. Kilic *et al* [7] recently introduced a volume integration scheme based on the collocation method. In this scheme, the Gaussian integration method with shape function transformation [8] is used to solve the volume integration over every subdomain. The work presented here employs an adaptive integration with error control. This method bears some resemblance to the recent advances on XFEM method in that both identify the intersection configurations of cutter interfaces/elements and cut elements [15–17].

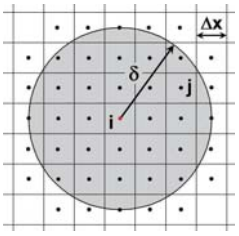

Figure 2: Modified accounting of family nodes (solid dots) by the adaptive integration.

The new integration method proposed here is focused on a more accurate numerical integration of Eqn. (12), *i.e.*, the integration is calculated over the intersection volume with controlled accuracy. For convenience, the new integration method is referred to as *adaptive integration*.

4.1 Modification of Counting the Family Nodes

To integrate Eqn. (12) accurately, the family nodes must be counted properly. Besides all the nodes fully in the horizon sphere, the adaptive integration also considers those nodes which are *out of the horizon sphere yet with cell volumes intersecting the horizon sphere* as family nodes. For every node, the shortest distance from the source node to the cell associated with that node is calculated. If the distance is smaller than the horizon, then the cell has volume inside the horizon sphere and the node is considered a family node. The newly-evaluated family nodes are shown in Fig. 2.

4.2 Categorization of Geometric Configurations

The integration limits in three directions need to be determined to evaluate the integral in Eqn. (12). For cells fully inside the horizon sphere the integration limits in the X (Y, or Z) direction are simply the coordinates of projection of the two opposite cell walls normal to X (Y, or Z) onto the X (Y, or Z) axis. For cells partially inside the horizon sphere, the limits are more difficult to calculated and are described in detail below. Two terms are defined: *family coordinate* is referred to as the local coordinate centered at the source node, and *first octant* is referred to as the octant where all three family coordinates are positive. Various possibilities of geometric configuration are classified into two categories as follows.

ISBN: 978-988-18210-0-3
ISSN: 2078-0958 (Print); ISSN: 2078-0966 (Online)

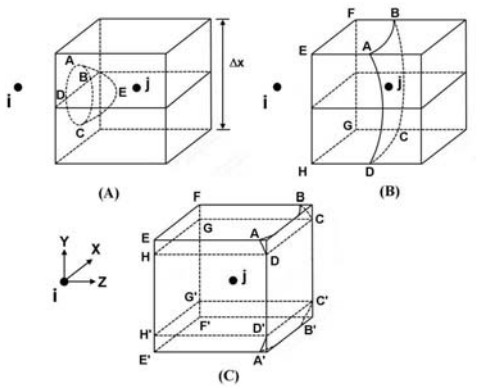

Figure 3: Possible geometric configurations for three subtypes of type one. (A) Subtype 1; (B) Subtype 2; (C) Subtype 3.

4.2.1 Geometric Configuration Type One

This type is for the configuration when *the family node is located on one axis of the family coordinate*. Without loss of generality, assume node j is in the first octant of the global coordinate system and on the Z+ axis of the family coordinate. If the global coordinates of the source node i and family node j are given as $(x_1^i,\, x_2^i,\, x_3^i)$ and $(x_1^j,\, x_2^j,\, x_3^j)$ respectively, then with the given assumption, $x_1^i = x_1^j,\, x_2^i = x_2^j$.

There are three subtypes of possible configurations between node i and j. Figure 3 depicts one possible geometric configuration for each subtype. Subtype 1 is chosen to illustrate the sequence of finding the integration limits. As shown in Fig. 3A, the intersection volume is formed by vertices *A-B-C-D-E*. The integration is carried out by integrating the Z direction first and the X direction last. The equation of circle *A-B-C-D* and the X coordinates of points B and D need to be solved to define the integration limits of X and Y directions. After they are solved, the integration of Eqn. (12) for the geometric configuration shown in Fig. 3A is expressed as:

$$I = \int_{x_1^B}^{x_1^D} \int_{x_2^i - \sqrt{\delta^2-(x_3^j-x_3^i-0.5\Delta x)^2-(X-x_1^i)^2}}^{x_2^i+\sqrt{\delta^2-(x_3^j-x_3^i-0.5\Delta x)^2-(X-x_1^i)^2}} \times \int_{x_3^j-0.5\Delta x}^{x_3^i+\sqrt{\delta^2-(X-x_1^i)^2-(Y-x_2^i)^2}} \mathbf{f}(\boldsymbol{\eta},\, \boldsymbol{\xi})\, dxdydz \qquad (15)$$

where $dxdydz$ is the infinitesimal volume associated with the integration point within the intersection volume.

4.2.2 Geometric Configuration Type Two

This type is for the configuration when *the family node is not located on any axis of the family coordinate*. Figure 4 shows one possible configuration for this type. The intersection volume is formed by vertices *A-B-C-D-E-F-G-K-L*. Based on the figure, the integration can be divided into two parts: part 1 integrates over the volume formed by vertices *A-B-C-D-E-F-G-F′-E′-L*, part 2 integrates over the volume formed by vertices *F-E-M-F′-E′-K*. After all the integration limits are solved, the integration can be carried out readily.

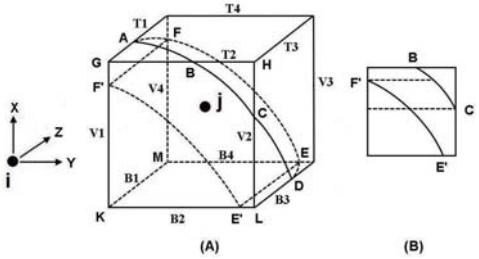

Figure 4: One possible geometric configuration for type two. (A) 3D view; (B) Projection onto the front face of the cell.

4.3 Adaptive Integration Using the Trapezoidal Rule with Error Control

Because of its simplicity and ease of error control, the composite trapezoidal rule [18] is used to carry out the preceding integrations. For the 1D case, it is stated as:

$$\int_a^b f(x)\, dx \approx \frac{b-a}{n} \times \left[\frac{f(a)+f(b)}{2} + \sum_{k=1}^{n-1} f\left(a + k\frac{b-a}{n}\right) \right] \qquad (16)$$

where the integer n is referred to as the *trapezoidal index*. The composite trapezoidal rule is used to achieve piecewise approximation of the curved surface of the intersection volume. The accuracy can be easily improved by adding more trapezoidal points into the calculation, i.e., by increasing the value of n. By applying the composite trapezoidal rule to each direction of the aforementioned 3D integrations (such as Eqn. (15)), the position of the integration points can be found.

A combined relative-absolute error control is used to achieve the prescribed accuracy. If the value of integration from the current iteration is denoted as I_r where r is the current step, and the value from the previous iteration is denoted as I_{r-1}, the error control scheme is stated as the following pseudo code:

if $(abs(I_{r-1}) > TOL)$
  if $(abs(I_r - I_{r-1}) <= EPS \cdot abs(I_{r-1}))$
    return I_r
else
  if $(abs(I_r - I_{r-1}) <= EPS)$
    return I_r

where $abs(\cdot)$ indicates the absolute value, EPS is the prescribed accuracy, and TOL is a pre-defined tolerance to prevent the dead lock when the integrand is very close to zero. A typical value of TOL is chosen to be 1.0×10^{-4}.

ISBN: 978-988-18210-0-3
ISSN: 2078-0958 (Print); ISSN: 2078-0966 (Online)

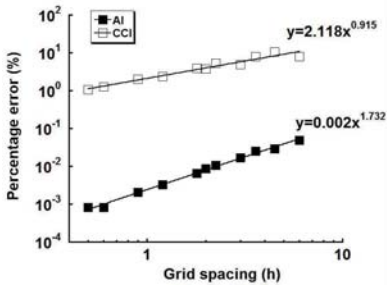

Figure 5: The convergence rates of the horizon sphere volume calculation by two integration methods.

Table 1: The volume of horizon sphere calculated by two volume integration methods.

Grid spacing $[h]$	AI (error) $[h^3][\%]$	CCI (error) $[h^3][\%]$
$\delta/3$	24416.9 (0.050)	22476.7 (7.992)
$\delta/4$	24421.8 (0.029)	21857.9 (10.525)
$\delta/5$	24422.8 (0.025)	22483.1 (7.976)
$\delta/6$	24424.9 (0.017)	23234.1 (4.891)
$\delta/8$	24426.4 (0.011)	23117.8 (5.367)
$\delta/9$	24426.9 (0.009)	23507.4 (3.773)
$\delta/10$	24427.4 (0.007)	23485.6 (3.862)
$\delta/15$	24428.2 (0.003)	23839.0 (2.415)
$\delta/20$	24428.5 (0.002)	23933.7 (2.028)
$\delta/30$	24428.8 (0.001)	24123.5 (1.251)
$\delta/36$	24428.8 (0.001)	24168.5 (1.066)

The adaptive integration scheme developed in this work can evaluate an integration with controlled accuracy. The convergence speed is proved to be close to quadratic (i.e., $O(\Delta x^2)$) and the error control method is quite effective.

5 Numerical Results

5.1 The Volume of the Horizon Sphere

In this example, the adaptive integration (AI) and cubic-cell integration (CCI) are used to calculate the volume of the horizon sphere of a source node. As only a finite array of nodes is used in the simulation, the source node is chosen at or near the center of the array so that its horizon sphere is fully inside the array. For example, in a uniform grid with $\Delta x = \delta/3$ as shown in Fig. 2, node i is the source node which has a total of 250 family nodes. Various grid spacings with a fixed horizon are used to investigate the rate of convergence, defined as the slope of the relative error-grid spacing plot, for both methods.

The physical length unit is denoted as h in the following calculations. The horizon is fixed to $18h$ so that the accurate volume of the horizon sphere is $4\pi R^3/3$ (or $24429.0h^3$). Table 1 compares the results by the AI and CCI methods with grid spacing ranging from $\Delta x = \delta/3$ to $\Delta x = \delta/36$. The rates of convergence for the two methods are shown in Fig. 5. Both methods become more accurate as the grid gets finer. The results by the AI method match the accurate volume very well (within 0.05%) even at the coarsest grid ($\Delta x = \delta/3$) and maintain a convergence rate of 1.73. For a given grid spacing Δx, the AI method is 2 to 3 orders of magnitude more accurate than the CCI method. Obvious fluctuations during the grid refinement (at $\Delta x = \delta/4$ and $\Delta x = \delta/8$) are observed from the results by the CCI method, which is possibly caused by the deficiencies discussed in Section 3.

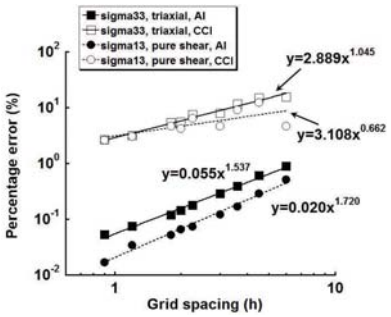

Figure 6: The convergence rates of σ_{33} in triaxial stress state and σ_{13} in pure shear for two integration methods.

5.2 Infinite Body Under Two Stress States

In this example, the areal force densities at a source node under triaxial (σ_{11}=$100N/h^2$, σ_{22}=$-150N/h^2$, σ_{33}=$220N/h^2$) and pure shear (σ_{13}=$200N/h^2$) stress states for an infinite body are calculated by both the AI and CCI methods and are compared with the closed form solutions. Various grid spacings with a fixed horizon are used to investigate the rate of convergence for both methods.

For example, for a grid spacing of $\Delta x = \delta/3$, a uniform gird of $10\times10\times10$ nodes is created and the node near the center of the domain at the coordinate of ($\Delta x/2$, $\Delta x/2$, $\Delta x/2$) is chosen to be the source node. The displacement of every node is prescribed according to the displacement solution of an infinite body for the given stress state. Consequently, this finite domain behaves like an infinite body. By assuming small deformation and linear elastic response, the closed form solution for stress at every node can be solved using classic elasticity theory.

A PMB material with Young's modulus of $1.0\times10^5 N/h^2$ is used. The horizon is fixed at $18h$ for all the calculations. For the AI method, the tolerance TOL is chosen to be 1.0×10^{-4}. The areal force density at the source node is calculated based on Eqn. (10).

The convergence rates of the largest principle stress σ_{33} in the triaxial stress state for both methods are shown in Fig. 6. The AI method shows a convergence rate of 1.53 with an error of 0.05% at $\Delta x = \delta/20$. The CCI method has a relatively flat convergence rate of 1.04 with an error of 2.64% at $\Delta x = \delta/20$.

ISBN: 978-988-18210-0-3
ISSN: 2078-0958 (Print); ISSN: 2078-0966 (Online)

The convergence rates of σ_{13} in the pure shear stress state for both methods are shown in Fig. 6. The AI method shows a convergence rate of 1.72 with an error of 0.017% at $\Delta x = \delta/20$. The CCI method shows obvious fluctuating trend as the grid gets finer and exhibits slow convergence rate of 0.66 in the pure shear stress state.

6 Conclusions

Integration plays an important role in the formulation of peridynamics. Published cubic-cell integration method in the literature, however, gives relatively low accuracy and the convergence rate with mesh refinement is low, in the range of 0.66 to 1.04 for the examples tested. The study here presents a new adaptive integration method with error control. The adaptive integration method improves the numerical implementation of bond-based peridynamics in the following ways:

1. The way to count the family nodes is modified to include all the material points in the whole horizon sphere.
2. A systematic categorization of geometric configuration for the intersection volume between the cell of a family node and the horizon sphere of the source node is developed so that accurate integration over the intersection volume becomes possible.
3. Adaptive trapezoidal quadrature with a combined relative-absolute error control is introduced into the new integration method for achieving numerical integration with desired accuracy.
4. Examples show results produced by the new adaptive integration method match the closed form solutions quite well even at the coarsest grid. The tested examples show the new adaptive integration method has high convergence rates (in the range of 1.53 to 1.72, or nearly quadratic, for the examples tested) and is both accurate and efficient.

References

[1] Silling, S.A., "Reformulation of Elasticity Theory for Discontinuities and Long-Range Forces," *J. Mech. Phys. Solids*, V48, N1, pp.175–209, 1/00.

[2] Silling, S.A., Askari, E., "Peridynamic Modeling of Impact Damage," 2004 ASME/JSME Pressure Vessels and Piping Conf, San Diego, USA, pp.197–205, 7/04.

[3] Xu, J., Askari, A., Weckner, O., Silling, S.A., "Peridynamic Analysis of Impact Damage in Composite Laminates," *J. Aerosp. Eng.*, V21, N3, pp.187–194, 7/08.

[4] Silling, S.A., Askari, E., "A Meshfree Method Based on the Peridynamic Model of Solid Mechanics," *Comput. Struct.*, V83, N17, pp.1526–1535, 6/05.

[5] Silling, S.A., Bobaru, F., "Peridynamic Modeling of Membranes and Fibers," *Int. J. Nonlin. Mech.*, V40, N2–3, pp.395–409, 3/05.

[6] Gerstle, W., Sau, N., Silling, S.A., "Peridynamic Modeling of Concrete Structures," *Nucl. Eng. Des.*, V237, N12–13, pp.1250–1258, 7/07.

[7] Kilic, B., Madenci, E., "Structural Stability and Failure Analysis Using Peridynamic Theory," *Int. J. Non-Linear Mech.*, V44, N8, pp.845–854, 10/09.

[8] Kilic, B., Agwai, A., Madenci, E., "Peridynamic Theory for Progressive Damage Prediction in Center-cracked Composite Laminates," *Compos. Struct.*, V90, N2, pp.141–151, 9/09.

[9] Silling, S.A., Lehoucq, R.B., "Convergence of Peridynamics to Classical Elasticity Theory," *J. Elast.*, V93, N1, pp.13–37, 10/08.

[10] Bobaru, F., Yang, M., Alves, L.F., Silling, S.A., Askari, E., Xu, J., "Convergence, Adaptive Refinement, and Scaling in 1D Peridynamics," *Int. J. Numer. Methods Eng.*, V77, N6, pp.852–877, 2/09.

[11] Silling, S.A., Epton, M., Weckner, O., Xu, J., Askari, E., "Peridynamic States and Constitutive Modeling," *J. Elast.*, V88, N2, pp.151–184, 8/07.

[12] Foster, J.T., Silling, S.A., Chen, W.W., "State Based Peridynamic Modeling of Dynamic Fracture," SEM Annual Conf and Exposition on Experimental and Applied Mechanics, Albuquerque, USA, pp.2312–2317, 6/09.

[13] Warren, T.L., Silling, S.A., Askari, A., Weckner, O., Epton, M.A., Xu, J., "A Non-ordinary State-based Peridynamic Method to Model Solid Material Deformation and Fracture," *Int. J. Solid. Struc.*, V46, N5, pp.1186–1195, 3/09.

[14] EMU Website, http://www.sandia.gov/emu/emu.htm.

[15] Fries, T.P., "A Corrected XFEM Approximation Without Problems in Blending Element," *Int. J. Numer. Methods Eng.*, V75, N5, pp.503–532, 7/08.

[16] Tabarraei, A., Sukumar, N., "Extended Finite Element Method on Polygonal and Quadtree Meshes," *Comput. Meth. Appl. Mech. Eng.*, V197, N5, pp.425–438, 1/08.

[17] Mayer, U.M., Gerstenberger, A., Wall, A.W., "Interface Handling for Three-dimensional Higher-order XFEM-computations in Fluid-structure Interaction," *Int. J. Numer. Methods Eng.*, V79, N7, pp.846–869, 8/09.

[18] Press, W.H., Teukolsky, S.A., Vetterling, W.T., Flannery, B.P., *Numerical Recipes in C*, 2nd Edition, Cambridge University Press, 1992.

ISBN: 978-988-18210-0-3
ISSN: 2078-0958 (Print); ISSN: 2078-0966 (Online)